Chemical Science

ROYAL SOCIETY OF CHEMISTRY

EDGE ARTICLE

View Article Online
View Journal | View Issue

Cite this: *Chem. Sci.*, 2024, **15**, 14924

All publication charges for this article have been paid for by the Royal Society of Chemistry

Received 5th June 2024
Accepted 9th August 2024

DOI: 10.1039/d4sc03688c

rsc.li/chemical-science

A thiol-triggered croconaine–chromene integration to induce ferroptosis and photothermal synergistic efficient tumor ablation†

Xinya Niu,[a] He Yang,[a] Xingkang Wu,[c] Fangjun Huo,[b] Kaiqing Ma *[ad] and Caixia Yin *[a]

Theranostic probes, combining diagnostic and treatment capabilities, have emerged as promising tools in tumor precision medicine. However, existing probes with constant fluorescence and photothermal activity can result in low signal-to-background ratios and phototoxicity. In this study, we introduced **CM-Croc**, a novel probe comprised of chromene and croconaine, selectively triggered by thiol. **CM-Croc** exhibited turn-on fluorescence and released croconaine for photothermal therapy. The croconaine moiety possesses high photothermal conversion efficiency up to 55%. Besides, it demonstrated potent activity against various cancer cell lines at low micromolar concentrations, including drug-resistant variants, through enhanced photothermal therapy combined with the ferroptosis effect. What's more, **CM-Croc** was proved to inhibit the activity of GPX4 to induce ferroptosis. Finally, **CM-Croc** was demonstrated to be the first croconaine-derived SOP, which targeted tumors and significantly inhibited tumor growth *in vivo* following intravenous administration with irradiation. This study showed **CM-Croc**'s potential for enhancing tumor precision medicine.

Introduction

Photothermal therapy (PTT), a method that harnesses the absorption and conversion of light to induce hyperthermia for cancer cell destruction, has gained prominence as a noninvasive strategy in cancer treatment,[1,2] especially for drug-resistant tumors.[3] The integration of tumor- and organelle-targeted small organic photothermal agents (SOPs) has demonstrated effective tumor inhibition during PTT.[4–6] Remarkably, Tang and colleagues have developed novel dual-targeted SOPs as PTT agents by targeting tumor tissue and mitochondria for fluorescence imaging (FI) of the tumor and selectively killing cancer cells.[7] However, the "always-on" approach in PTT probes has raised concerns, leading to adverse effects such as thermal damage to normal tissues, inflammation, and patient discomfort (Fig. 1).[8,9] Moreover, the energy is limited for the fluorescence and photothermal effect when only one dye absorbs a photon. Although activable (off–on) photosensitizers have been developed for photodynamic therapy (PDT),[10–12] activable PTT probes, especially those utilizing SOPs, have received limited attention.[13,14] Additionally, the activation for photoacoustic imaging (PAI) has been reported,[15] which could be combined with the photothermal effect for diagnosis and therapy.[16] Despite this promising synergy, PAI generally exhibits lower sensitivity and specificity compared to fluorescence imaging (FI). Furthermore, the complexity of data interpretation in PAI poses additional challenges. Simultaneously, significant efforts have been directed toward combining PTT with the inhibition of heat shock protein (HSP) expression to enhance the therapeutic efficacy of the photothermal effect.[17] Notably, the upregulation of intracellular reactive oxygen species (ROS) during the process of ferroptosis offers a pathway for inhibiting HSP expression. As a result, the combined approach of ferroptosis and PTT is proposed as a promising strategy for effectively targeting cancer cells.[18,19]

Croconaine (Croc) compounds belong to the donor–acceptor–donor (D–A–D) class of zwitterionic molecules with an intense absorption in the near-infrared (NIR) region and high thermal efficiency, especially in acid environments.[20,21] Despite their considerable potential for bioimaging applications, the intrinsic instability stemming from self-aggregation and the limited tumor-targeting capability of Croc have constrained their broad biomedical utilization *in vivo*.[22,23] To address these limitations, chemical conjugation techniques have been extensively employed to enhance the physicochemical properties and

[a]*Key Laboratory of Chemical Biology and Molecular Engineering of Ministry of Education, Institute of Molecular Science, Shanxi University, Taiyuan 030006, PR China. E-mail: yincx@sxu.edu.cn*

[b]*Research Institute of Applied Chemistry, Shanxi University, Taiyuan 030006, PR China*

[c]*Modern Research Center for Traditional Chinese Medicine, Shanxi University, Taiyuan 030006, China*

[d]*Zhendong Research Institute, Shanxi-Zhendong Pharmaceutical Co., Ltd, Changzhi 047100, China*

† Electronic supplementary information (ESI) available. See DOI: https://doi.org/10.1039/d4sc03688c

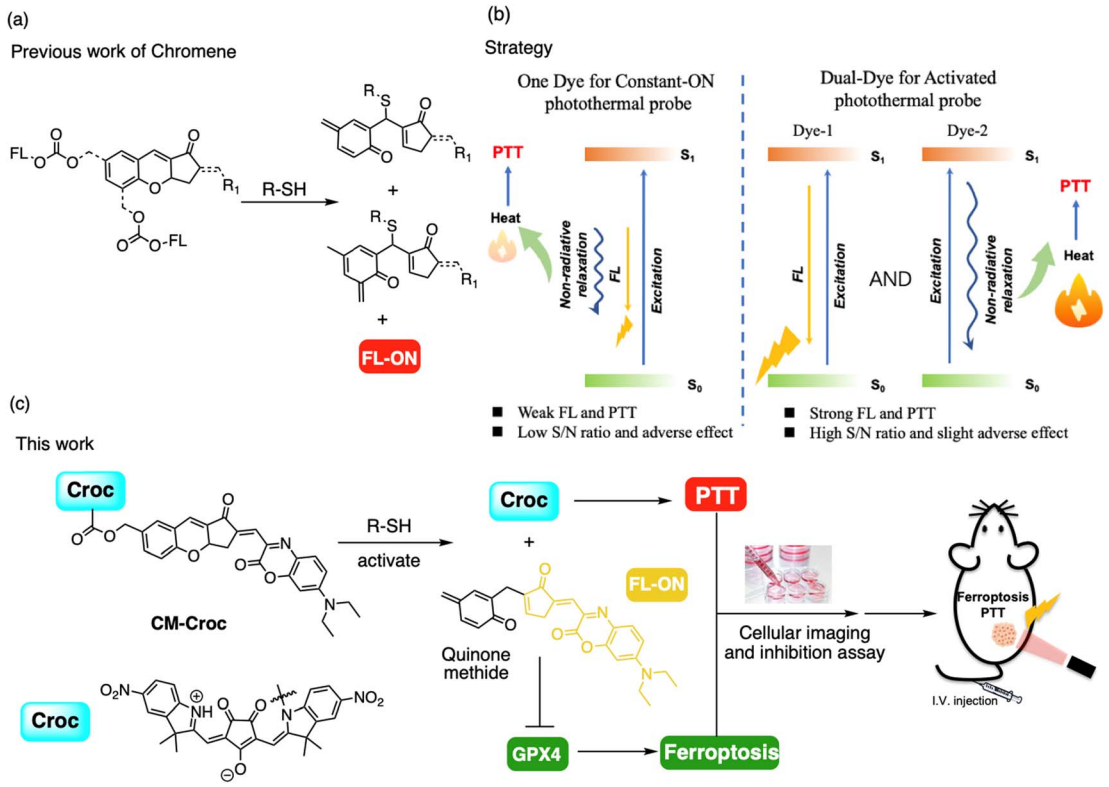

Fig. 1 (a) Previous work: thiol-mediated nucleophilic attack on unsaturated α,β-ketone. (b) The dual-dye for an activated photothermal probe strategy. (c) Schematic illustration for the assembly of chromene and croconaine to afford **CM-Croc** facilitating a novel approach to combined chemotherapy and thermotherapy.

functionalities of Croc.[24] However, it is noteworthy that the introduction of chemical conjugation may compromise the thermostability of Croc when applied to photothermal therapy.

Our recent work has focused on the development of a thiol–chromene "click" nucleophilic reaction, resulting in the creation of a turn-on probe for thiol detection with remarkable selectivity and high signal-to-background ratios.[25–28] Additionally, in our previous studies,[29,30] we extended the utility of the thiol-triggered cascade reaction to generate quinone methide and release functional components, such as near-infrared (NIR) fluorophores and organelle targeting groups. Building upon this foundation, we envisioned the prospect of integrating the chromene component with the Croc structure to produce a thiol-responsive probe. This hybrid probe not only facilitated high signal-to-background ratio fluorescence imaging but also activated the Croc moiety for PTT. Importantly, quinone methide (QM) generated in this cascade reaction was postulated to inhibit glutathione peroxidase 4 (GPX4) and induce ferroptosis.[31] The high level of thiol in the tumor region could facilitate the controlled release of *p*-quinone methide and Croc,[32] enabling a combined approach involving both chemotherapy and thermotherapy.

As a proof-of-concept, we engineered probe **CM-Croc** by combining chromene and Croc for a novel approach to integrated photothermal therapy and ferroptosis-based cancer theranostics. **CM-Croc** demonstrated the ability to effectively penetrate cells and selectively target thiol in the mitochondria. Moreover, when administered intravenously, **CM-Croc** exhibited a remarkable propensity to accumulate in tumor regions, enabling clear differentiation between the tumor and normal tissue based on thiol levels, thus achieving high contrast. Notably, our research showed the release of QM, which was found to inhibit GPX4 activity and induce ferroptosis. The anticancer effect was significantly enhanced when combined with irradiation, particularly against HCT-116 and drug-resistant cell lines (HT-29, HCT116 $p53^{-/-}$), achieving potent inhibition at low micromolar concentrations. Furthermore, **CM-Croc** demonstrated outstanding *in vivo* therapeutic efficacy through the combination of PTT and ferroptosis induction. Importantly, to the best of our knowledge, **CM-Croc** represents the first application of a Croc-derived SOP for *in vivo* photothermal therapy through intravenous administration. Overall, our work has introduced a robust and reliable tool for advancing theranostic research in the field of cancer treatment.

Results and discussion

Probe design and synthesis

In our previous investigation, we synthesized the chromene structure from (2-hydroxy-5-methyl-1,3-phenylene) dimethanol, employing a two-step synthesis approach (Scheme S1†).[26] Subsequently, we chose the coumarin moiety as the candidate for condensation with chromene, resulting in the formation of compound **4** under established reaction conditions.[27] Notably,

the structural substitution of oxygen with nitrogen within coumarin moiety **4** led us to anticipate an extended emission wavelength compared to our previous findings. Compound **4** was then subjected to a reaction with triphosgene and Croc (**5**) to provide the final probe **CM-Croc** (**1**) with a moderate yield.

Spectral properties

The assessment of **CM-Croc**'s capacity to release the chromene–coumarin moiety was conducted through the examination of UV-vis absorption and fluorescence spectra (Fig. 2a, b and S1†). Notably, the absorption peak at 700 nm exhibited a substantial increase upon the introduction of thiol compounds, suggesting the liberation of the Croc moiety in comparison to the absorption profile of Croc in isolation (Fig. S2†). It is noteworthy that while the absorbance behaviour appeared typical under standard conditions, a noteworthy enhancement was expected under the acidic milieu characteristic of tumor regions, in line with previous findings.[33] A conspicuous fluorescence "turn-on" effect at 580 nm from the coumarin part was observed upon interaction with thiols through the mechanism reported in our previous work.[30] However, the emission wavelength was notably shorter than that of the substructure devoid of the Croc component (Fig. S3†). Additionally, kinetic investigations revealed the completion of the reaction within a period of 30(34) minutes (Fig. 2c). Intriguingly, in contrast to our previously developed probe,[29,30] the reaction rate of **CM-Croc** was comparatively sluggish. Based on these two sets of results, it was postulated that a direct interaction occurred between the Croc moiety and the chromene–coumarin segment. Subsequently, the selectivity of **CM-Croc** for thiols was scrutinized (Fig. 2d). The results indicated that only thiol elicited significant alterations in fluorescence emission at 580 nm.

Subsequently, we investigated the photophysical attributes of **CM-Croc**, with a particular focus on its photothermal effect. Employing 660 nm laser irradiation at a power density of 0.35 W cm^{-2}, we observed a rapid elevation in temperature change within the **CM-Croc** aqueous solution, reaching 70 °C within the initial 10 minutes subsequent to thiol treatment, as illustrated in Fig. 3a and S4.† Conversely, when the photothermal effect was examined in the absence of cysteine (Cys), the results indicated an insignificant temperature change when compared to the Cys-treated group (Fig. S5†). To provide a quantitative assessment of the photothermal conversion efficiency (PCE), we calculated it to be approximately 55% based on the observed photothermal effects and time constants, as depicted in Fig. S6.† It is noteworthy that this PCE value for **CM-Croc** surpasses the majority of previously reported small molecular photothermal agents, including ICG (~3.1%) (Table S1†).[34] Furthermore, we explored the concentration and power density-dependent photothermal efficiency of **CM-Croc**, affirming its versatility and potential efficacy (Fig. 3b and c). In addition to these observations, we examined the stability of **CM-Croc**, a pivotal factor for an effective photothermal probe. Following irradiation with a 660 nm laser for three on–off cycles, **CM-Croc** (at a concentration of 100 μM) consistently maintained a maximum temperature of around 70 °C, thus underscoring its remarkable photothermal stability (Fig. 3d). These cumulative findings emphasize the promising photothermal properties of **CM-Croc**, positioning it as a noteworthy candidate for effective photothermal therapy.

Next, the ability of probe **CM-Croc** to penetrate the cell membrane was evaluated (Fig. S7†). The results indicated that

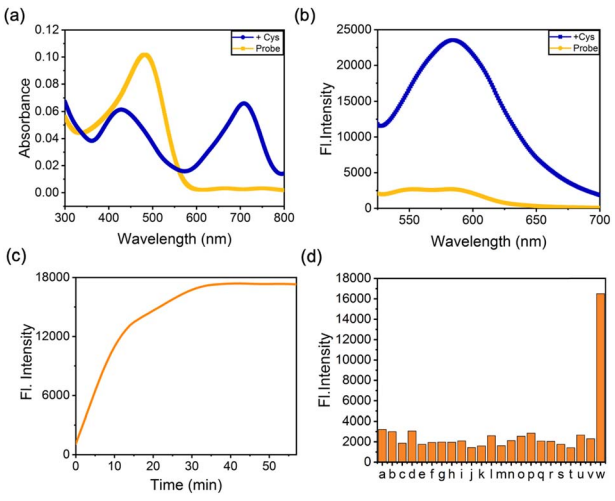

Fig. 2 Optical responses of **CM-Croc** to thiol (a) absorption changes of **CM-Croc** (10 μM, EtOH : PBS, 1 : 1, v/v) after adding 200 μM Cys. (b) Fluorescence intensity changes of probe **CM-Croc** (10 μM, EtOH : PBS, 1 : 1, v/v) with the addition of 200 μM Cys after 40 min; (λ_{ex} = 500 nm, slit: 10 nm/10 nm). (c) The kinetic curve of **CM-Croc** (10 μM) in the mixed solvent of EtOH and PBS (1 : 1, v/v) with 200 μM Cys at 580 nm (slit: 10 nm/10 nm). (d) Fluorescent intensity responses of **CM-Croc** (10 μM, PBS : EtOH, 1 : 1, v/v) to various ions and amino acid at 580 nm. Including: a to w represent Ca^{2+}, F^{-}, Fe^{2+}, HCO_3^{-}, K^{+}, Mg^{2+}, NH_4^{+}, NO_2^{-}, OH^{-}, SCN^{-}, SO_3^{2-}, Zn^{2+}, Cu^{2+}, Pro, Gly, Glu, H_2O_2, Arg, Lys, GABA, Asn, His, Cys.

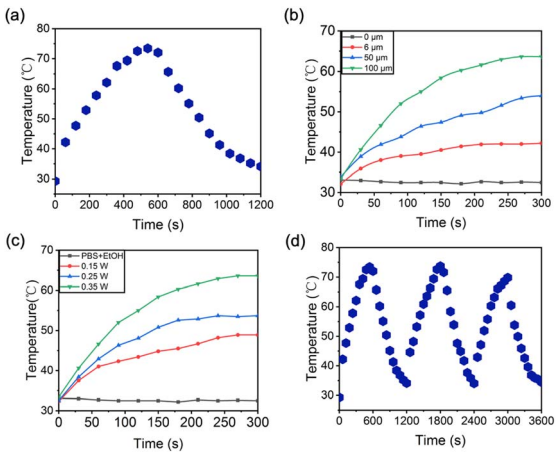

Fig. 3 Photophysical properties of **CM-Croc** in the presence of thiol. (a) Detection of cooling points. (b) Temperatures of **CM-Croc** with various concentrations in a mixture of ethanol and PBS buffer (1 : 1, v/v) under irradiation (660 nm, 0.35 W cm^{-2}). (c) Temperatures of **CM-Croc** (100 μM) under various laser densities (0.35 W cm^{-2}) in a mixture of ethanol and PBS buffer (1 : 1, v/v). (d) Temperature variations of **CM-Croc** (100 μM) under irradiation (660 nm, 0.35 W cm^{-2}) for three laser on/off cycles.

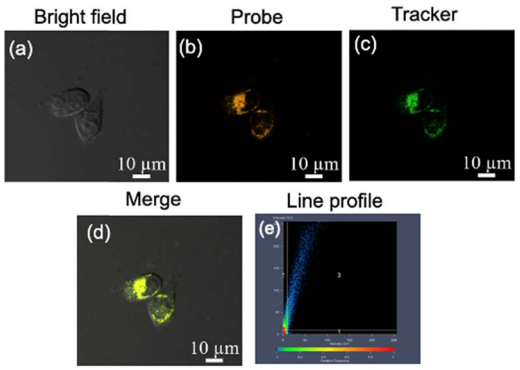

Fig. 4 Confocal fluorescence images of HeLa cells co-stained with **CM-Croc** and a tracker. (a and b) Cells pretreated with **CM-Croc** (10 μM) for 20 min and subsequently Mito-Tracker Green (1 μM) at 37 °C for 30 min. λ_{ex} = 500 nm and λ_{em} 563–593 nm. (c) Fluorescence images from Mito-Tracker Green, λ_{ex} 488 nm and λ_{em} 500–540 nm. (d) Overlay of the orange and green channels. (e) Intensity scatter plot of Mito-Tracker Green and **CM-Croc**. Scale bars: 10 μm.

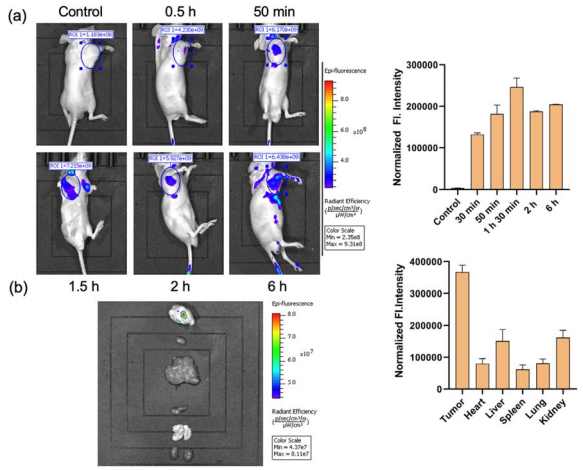

Fig. 5 Fluorescence imaging of nude mice bearing HCT-116 tumors after intravenous injection of **CM-Croc** at various time points. (a) Changes in fluorescence intensity over time. (b) Fluorescence imaging of each organ and tumor after dissecting the mouse. Data are represented as mean ± SD (n = 3).

probe **CM-Croc** could enter the cell well. Moreover, when the cells were pretreated with *N*-methylmaleimide or exogenous, the intracellular fluorescence decreased or increased, respectively, which indicated that fluorescence occurred after **CM-Croc** reacted with the thiols in the living cells. Subsequently, the colocalization experiment was conducted. It is surprising that probe **CM-Croc** selectively localized in mitochondria (Fig. 4) and the Pearson's coefficient is around 0.90, which was probably due to the nitrogen heterocycles with N–H bonds.[35]

Imaging in cells and tumors

In the subsequent phase of our investigation, we aimed to assess the viability of imaging of tumors with **CM-Croc**. To accomplish this, we intravenously administered **CM-Croc** to BALB/c nude mice with subcutaneous HCT-116 tumors. Subsequent to the administration, we observed a discernible fluorescence signal within the tumor tissue as early as 1 hour post-injection. This signal reached its peak intensity at approximately 1.5 hours post-injection (Fig. 5a). Following this, the experimental mouse was euthanized, and the associated fluorescence imagery unambiguously delineated the tumor (Fig. 5b). Notably, our findings revealed that other organs exhibited relatively weaker fluorescence signals, with the liver being one such example. This observation was in alignment with our initial hypothesis, substantiating the notion that **CM-Croc** possesses the capability to accumulate within the tumor region. Moreover, it shows **CM-Croc**'s potential to effectively discriminate between tumor and normal tissues based on variations in thiol levels.

Subsequently, ES-2 cells were subjected to initial treatment with **CM-Croc**, alongside the use of the apoptosis inhibitor z-VAD-fmk (z-VAD) and the necroptosis inhibitor necrostatin-1 (Nec-1), as depicted in Fig. 6a. Notably, it was observed that the cytotoxicity induced by **CM-Croc** remained unmitigated by the presence of z-VAD and Nec-1, implying that **CM-Croc** did not influence apoptosis or necroptosis. Furthermore, when ES-2 cells were exposed to varying concentrations of **CM-Croc** for a duration of 24 hours, a dose-dependent inhibition of ES-2 cell viability was evident. In contrast, when ES-2 cells were co-incubated with **CM-Croc** and the ferroptosis inhibitor ferrostatin-1 (Fer-1), a substantial rescue of cell death was observed (Fig. 6b). This protective effect was also mirrored when

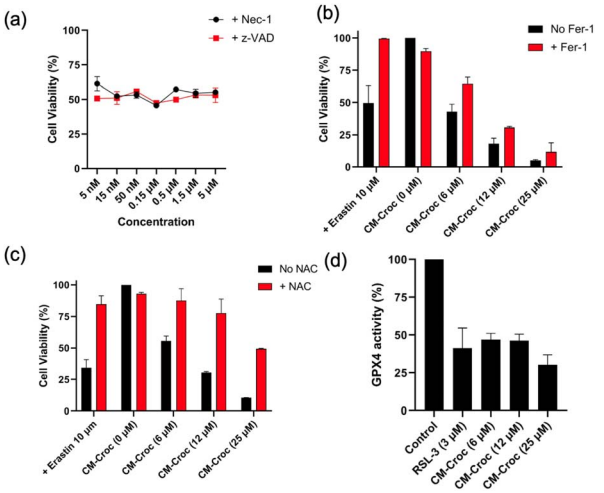

Fig. 6 **CM-Croc** induces ferroptosis. (a) The necrosis inhibitor Nec-1 in black and the apoptosis inhibitor z-VAD in red showed the protective ability of ES-2 cells treated with **CM-Croc** (6 μM) after 24 hours. (b) Black is the effect of **CM-Croc** (0, 6 μM, 12 μM, 25 μM) on the viability of ES-2 cells for 24 hours. Red indicates the effect of Fer-1 (2 μM) on the viability of ES-2 cells after 24 h of **CM-Croc** and erastin (10 μM). (c) Black is the effect of **CM-Croc** (0, 6 μM, 12 μM, 25 μM) on the viability of ES-2 cells for 24 hours. Red indicates the effect of NAC (1 mM) on the viability of ES-2 cells after 24 h of **CM-Croc** and erastin (10 μM). Data are expressed as mean ± SD (n = 3). (d) **CM-Croc** against GPX4 activity in ES-2 cells treated with RSL-3 (3 μM) and **CM-Croc**. Data are expressed as mean ± SD (n = 3).

N-acetyl cysteine (NAC), serving as an antioxidant, was introduced alongside **CM-Croc** (Fig. 6c). Notably, a parallel set of results were obtained when HCT-116 cells were exposed to **CM-Croc** (Fig. S8†). **CM-Croc** continued to exhibit substantial inhibitory effects on HCT-116 cells in a concentration-dependent manner, specifically through ferroptosis. Importantly, the positive control agents, erastin and RSL3, displayed negligible inhibitory effects on the growth of HCT-116 cells after 24 hours of treatment, which was consistent with the previous result.[36] Moreover, **CM-Croc** showed weak toxicity toward the normal colorectal cell NCM-460 even at 25 μM, which was probably due to the low level of thiol in the normal cells (Fig. S9†).

CM-Croc, by virtue of its ability to react with thiols and generate quinone methide, was postulated to exert inhibitory effects on GPX4. This led to the proposition that **CM-Croc** might induce redox dyshomeostasis and elevate intracellular oxidative stress, ultimately triggering ferroptosis. In order to scrutinize this hypothesis, we investigated the inhibitory effect of **CM-Croc** on GPX4 at cellular levels. As shown in Fig. 6d, the activity of the intracellular GPX4 enzyme treated with **CM-Croc** significantly decreased compared with that treated with positive control (RSL-3).

Afterward, we assessed the synergistic chemo- and photothermal toxicity of **CM-Croc** on HCT-116 cells *in vitro*. Prior to exposing HCT-116 cells to laser treatment, various laser power settings were tested (Fig. S10†). These preliminary experiments revealed a significant reduction in HCT-116 cell viability when the laser power was adjusted to 0.35 W cm^{-2}. Following this, HCT-116 cells were incubated with **CM-Croc** for a duration of 4 hours, while simultaneously subjecting them to laser irradiation at a power of 0.35 W cm^{-2} for 5 minutes. The results demonstrated that cell viability decreased in a concentration-dependent manner under these conditions. In contrast, the control group that did not receive laser treatment exhibited comparatively weaker inhibitory effects over the same 4 hour period (Fig. 7a). Additionally, it is noteworthy that drug-resistant colon cancer cell lines, including HCT-116 $p53^{-/-}$ and HT-29, also exhibited heightened sensitivity to the combined chemo- and thermotherapy, as illustrated in Fig. 7b and c. These findings underscore the enhanced efficacy of **CM-Croc** in inhibiting the growth of HCT-116 cells and its drug-resistant variants when subjected to combined chemo- and thermotherapy.

Building upon the promising results obtained from our *in vitro* experiments, we proceeded to investigate the *in vivo* anticancer potential of **CM-Croc**. To achieve this, we employed xenograft mouse models bearing HCT-116 cell-derived tumors. Initially, the *in vivo* photothermal effect of **CM-Croc** was explored under 660 nm laser excitation (0.2 W cm^{-2}) one hour after **CM-Croc** injection in an intravenous manner (as demonstrated in Fig. S11†). Notably, the temperature rapidly escalated from 35.6 °C to 64.7 °C within a span of 5 minutes (Fig. S12†). In contrast, the temperature changes in the PBS group and the Croc group were approximately 7.3 °C and 5.8 °C, respectively. These findings substantiate **CM-Croc**'s ability to accumulate at the tumor site and release croconaine for PTT.

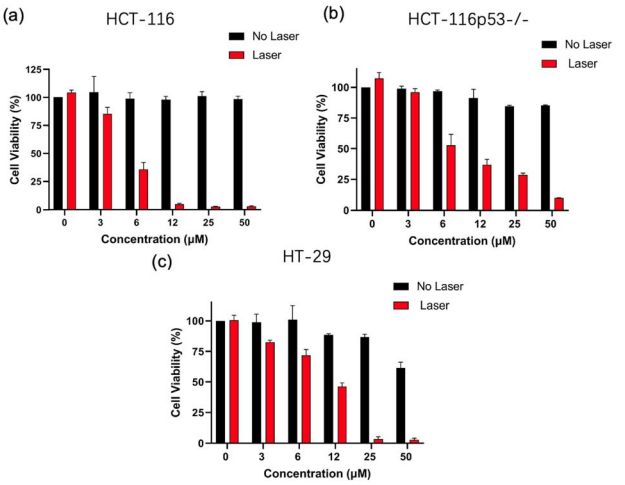

Fig. 7 The synergistic chemo- and photothermal toxicity of **CM-Croc**. (a) Black bars indicate the cell dark toxicity test of HCT-116 cells incubated at different concentrations of **CM-Croc** (0, 6 μM, 12 μM, 25 μM, 50 μM) for 4 hours, and red bars indicate HCT-116 cells incubated at different concentrations of **CM-Croc**, 0.35 W cm^{-2} 660 nm laser irradiation after 5 minutes of photothermal cytotoxicity. (b) and (c) show HCT-116 $p53^{-/-}$ and HT29 cells, and the rest are the same as above. Data are represented as mean ± SD ($n = 3$).

Subsequently, we evaluated the therapeutic impact on tumor growth by monitoring the tumor volume. As illustrated in Fig. 8, the control group (PBS and laser treatment) exhibited rapid tumor growth without significant inhibitory effects. In contrast, **CM-Croc** and Croc with the laser group displayed modest inhibitory effects, whereas **CM-Croc** and the laser group demonstrated substantial tumor suppression. These results emphasize the collaborative efficacy of the combined chemotherapy and photothermal therapy in more effectively and specifically inhibiting cancer cells.

In order to assess the biosafety and potential side effects of the photothermal agent, histological examination was

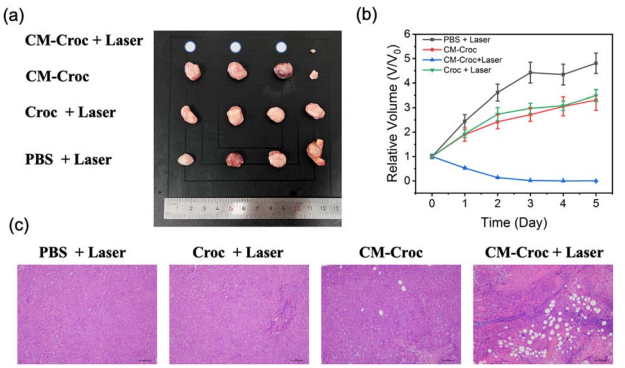

Fig. 8 Thiol-activated photothermal therapy with **CM-Croc** in HCT-116 tumor-bearing mice. (a) Tumor images of four groups of nude mice on day 6 after photothermal treatment. Data are expressed as mean ± SD ($n = 4$). (b) Tumor growth curves with time after different treatments. (c) H&E staining photos of tumors tissue in different treatment groups.

conducted on major organs, including the heart, liver, spleen, lung, kidney, and the tumor, after 5 days of treatment (as shown in Fig. S13†). The results revealed no observable necrosis or injury in the major organs. Notably, the tumor tissue displayed clear signs of necrosis in the **CM-Croc** and laser group. Furthermore, no significant fluctuations in body weight were observed during the five-day treatment, underscoring the excellent biosafety profile of **CM-Croc** (Fig. S14†). These findings support the potential of **CM-Croc** as a safe and effective approach for cancer treatment *in vivo*.

Conclusion

In summary, we have successfully developed a novel probe, **CM-Croc**, for the purpose of integrated photothermal and ferroptosis-based cancer theranostics. This probe responded to thiol activation, releasing croconaine and enabling the activation of fluorescence with high signal-to-background ratios. Importantly, **CM-Croc** exhibited exceptional PCE and maintained good photothermal stability. Additionally, **CM-Croc** possessed outstanding tumor-targeting capabilities, allowing for the clear differentiation of tumor tissue from normal tissue *in vivo* following intravenous administration. Furthermore, **CM-Croc** has been demonstrated to induce ferroptosis in a concentration-dependent manner through the inhibition of GPX4. Significantly, our findings reveal that cancer cell lines, including drug-resistant variants, exhibit heightened sensitivity to the combined chemo- and thermotherapy, even at low micromolar concentrations with low laser power. Finally, the synergistic anticancer effects of **CM-Croc** have been corroborated in a xenograft mouse model of tumors. This approach presents a promising strategy, offering the potential for the design of more adaptable and switchable photothermal probes, aimed at achieving combined chemo- and thermotherapy. These advancements hold substantial promise for the development of innovative and effective cancer treatment strategies.

Data availability

The authors confirm that the data supporting the findings of this study are available within the article. The supporting data include experimental procedures and analytical data (NMR and HRMS), which can be found in the ESI.† Copies of NMR spectra are also provided.

Author contributions

K. M. and C. Y. conceived the project. X. N. and H. Y. synthesized the dyes and conducted photophysical characterization and analysis. H. Y. and X. W. performed fluorescence imaging experiments. X. N. and F. H. characterized structures. All authors participated in writing the manuscript.

Conflicts of interest

There are no conflicts to declare.

Acknowledgements

We thank the National Natural Science Foundation of China (22077076, 22325703, 22377071, and U23A6009), the Research Project Supported by the Shanxi Scholarship Council of China (2023-012, 2022-002), the Shanxi Province Science Foundation (no. 202203021221009), and the Scientific Instrument Center of Shanxi University (201512).

Notes and references

1 X. Li, J. F. Lovell, J. Yoon and X. Chen, *Nat. Rev. Clin. Oncol.*, 2020, **17**, 657–674.
2 H. S. Jung, P. Verwilst, A. Sharma, J. Shin, J. L. Sessler and J. S. Kim, *Chem. Soc. Rev.*, 2018, **47**, 2280–2297.
3 L. B. Carpin, L. R. Bickford, G. Agollah, T. K. Yu, R. Schiff, Y. Li and R. A. Drezek, *Breast Cancer Res. Treat.*, 2011, **125**, 27–34.
4 X. Guo, N. Yang, W. Ji, H. Zhang, X. Dong, Z. Zhou, L. Li, H. Shen, S. Yao and W. Huang, *Adv. Mater.*, 2021, **33**, 2007778.
5 H. Jung, J. Lee, K. Kim, S. Koo, P. Verwilst, J. L. Sessler, C. Kang and J. Kim, *J. Am. Chem. Soc.*, 2017, **139**, 9972–9978.
6 R. Wang, X. Li and J. Yoon, *ACS Appl. Mater. Interfaces*, 2021, **13**, 19543–19571.
7 H. Wang, J. Chang, M. Shi, W. Pan, N. Li and B. Tang, *Angew. Chem., Int. Ed.*, 2019, **58**, 1057–1061.
8 X. Deng, Z. Shao and Y. Zhao, *Adv. Sci.*, 2021, **8**, 2002504.
9 M. Salimi, S. Mosca, B. Gardner, F. Palombo, P. Matousek and N. Stone, *Nanomaterials*, 2022, **12**, 922.
10 J. Tian, B. Li, F. Zhang, Z. Yao, W. Song, Y. Tang, Y. Ping and B. Liu, *Angew. Chem., Int. Ed.*, 2023, **135**, e202307288.
11 M. Zhao, Y. Zhang, J. Miao, H. Zhou, Y. Jiang, Y. Zhang, M. Miao, W. Chen, W. Xing, Q. Li and Q. Miao, *Adv. Mater.*, 2023, **36**, 2305243.
12 X. Chen, Z. Zhang, W. Luo, Z. Zhuang, Z. Zhao, L. Wang, D. Wang and B. Tang, *Biomaterials*, 2022, **287**, 121680.
13 X. Meng, J. Zhang, Z. Sun, L. Zhou, G. Deng, S. Li, W. Li, P. Gong and L. Cai, *Theranostics*, 2018, **8**, 6025–6034.
14 H. Han, H. Wang, P. Jangili, M. Li, L. Wu, Y. Zang, A. C. Sedgwick, J. Li, X. He, T. D. James and J. Kim, *Chem. Soc. Rev.*, 2023, **52**, 879–920.
15 H. Knox, T. Kim, Z. Zhu and J. Chan, *ACS Chem. Biol.*, 2018, **13**, 1838–1843.
16 Y. Liu, P. Bhattarai, Z. Dai and X. Chen, *Chem. Soc. Rev.*, 2019, **48**, 2053–2108.
17 X. Zhang, S.-S. Xue, W. Pan, H. Wang, K. Wang, N. Li and B. Tang, *Chem. Commun.*, 2023, **59**, 235–238.
18 M. Chang, Z. Hou, M. Wang, C. Yang, R. Wang, F. Li, D. Liu, T. Peng, C. Li and J. Lin, *Angew. Chem., Int. Ed.*, 2021, **60**, 12971–12979.
19 S. He, Y. Jiang, J. Li and K. Pu, *Angew. Chem., Int. Ed.*, 2020, **59**, 10633–10638.
20 S. Lei, Y. Zhang, N. T. Blum, P. Huang and J. Lin, *Bioconjugate Chem.*, 2020, **31**, 2072–2084.
21 Y. Wen, H. H. McGarraugh, C. L. Schreiber and B. D. Smith, *Chem. Commun.*, 2020, **56**, 6977–6980.

22 C. R. Ouyang, P. You, F. Lu, H. Mei, J. Yu, Z. Zhu and C. Zhou, *Dyes Pigm.*, 2024, **221**, 111780.
23 J. S. Al-Otaibi, Y. S. Mary, Y. S. Mary and R. Thomas, *Spectrochim. Acta, Part A*, 2022, **264**, 120233.
24 F. Zeng, L. Tang, Q. Zhang, C. Shi, Z. Huang, S. R. Y. Nijiati, X. Chen and Z. Zhou, *Angew. Chem., Int. Ed.*, 2022, **134**, e202112925.
25 K. Ma, L. Zhao, Y. Yue, F. Huo, J. Chao and C. Yin, *Anal. Chem.*, 2020, **92**, 15936–15942.
26 F. Huo, Y. Sun, J. Su, Y. Yang, J. Chao and C. Yin, *Org. Lett.*, 2009, **11**, 4918.
27 K. Ma, L. Zhao, Y. Yue and C. Yin, *Chem. Phys. Rev.*, 2022, **3**, 011302.
28 Y. Yang, K. Zhou, M. Ma, H. Liu, M. Jin, C. Yin, S. Wang and J. Zhang, *Chem. Eng. J.*, 2023, **452**, 139020.
29 Y. Yang, T. Zhou, M. Jin, K. Zhou, D. Liu, X. Li, F. Huo, W. Li and C. Yin, *J. Am. Chem. Soc.*, 2020, **142**, 1614–1620.
30 K. Ma, H. Yang, T. Shen, Y. Yue, L. Zhao, X. G. Liu, F. Huo and C. Yin, *Chem. Sci.*, 2022, **13**, 3706–3712.
31 D. Qi, L. Xing, L. Shen, W. Sun, C. Cai, C. Xue, X. Song, H. Yu, H. Jiang and C. Li, *Chin. Chem. Lett.*, 2022, **33**, 4595–4599.
32 Y. Wang, P. Pigeon, W. Li, J. Yan, P. M. Dansette, M. Othman, M. J. McGlinchey and G. Jaouen, *Eur. J. Med. Chem.*, 2022, **234**, 114202.
33 S. Guha, G. K. Shaw, T. M. Mitcham, R. R. Bouchard and B. D. Smith, *Chem. Commun.*, 2016, **52**, 120–123.
34 L. Weng and Y. Liu, *Drug Discov. Today*, 2021, **26**, 2045–2052.
35 W. Ma, B. Xu, R. Sun, Y. J. Xu and J. F. Ge, *J. Mater. Chem. B*, 2021, **9**, 2524–2531.
36 E. Llabani, R. W. Hicklin, H. Y. Lee, S. E. Motika, L. A. Crawford, E. Weerapana and P. J. Hergenrother, *Nat. Chem.*, 2019, **11**, 521–532.